Published in final edited form as:
Eur J Nucl Med Mol Imaging. 2016 November ; 43(12): 2169–2179. doi:10.1007/s00259-016-3442-1.

ImmunoPET for assessing the differential uptake of a CD146-specific monoclonal antibody in lung cancer

Haiyan Sun#1, **Christopher G. England**#2, **Reinier Hernandez**[2], **Stephen A. Graves**[2], **Rebecca L. Majewski**[3], **Anyanee Kamkaew**[1], **Dawei Jiang**[1], **Todd E. Barnhart**[2], **Yunan Yang**[1,*], and **Weibo Cai**[1,2,3,4,*]

[1]Department of Radiology, University of Wisconsin - Madison, WI 53705, USA

[2]Department of Medical Physics, University of Wisconsin - Madison, WI 53705, USA

[3]Department of Biomedical Engineering, University of Wisconsin - Madison, WI 53705, USA

[4]University of Wisconsin Carbone Cancer Center, Madison, WI 53705, USA

# These authors contributed equally to this work.

Abstract

Purpose—Overexpression of CD146 in solid tumors has been linked to disease progression, invasion, and metastasis. In this study, we describe the generation of a ^{64}Cu-labeled CD146-specific antibody for quantitative immunoPET imaging of CD146 expression in six lung cancer models.

Methods—The anti-CD146 antibody (YY146) was conjugated to 1,4,7-triazacyclononane-triacetic acid (NOTA) and radiolabeled with ^{64}Cu. CD146 expression was evaluated in six human lung cancer cell lines (A549, NCI-H358, NCI-H522, HCC4006, H23, and NCI-H460) by flow cytometry and quantitative Western blot studies. The biodistribution and tumor uptake of ^{64}Cu-NOTA-YY146 was assessed by sequential PET imaging in athymic nude mice bearing subcutaneous lung cancer xenografts. The correlation between CD146 expression and tumor uptake of ^{64}Cu-NOTA-YY146 was evaluated by graphical software while *ex vivo* biodistribution and immunohistochemistry studies were performed to validate the accuracy of PET data and spatial expression of CD146.

Results—Flow cytometry and Western blot studies showed similar findings with H460 and H23 cells highly expressing CD146. Small differences in CD146 expression levels were found between A549, H4006, H522, and H358 cells. Tumor uptake of ^{64}Cu-NOTA-YY146 was highest in CD146-expressing H460 and H23 tumors, peaking at 20.1 ± 2.86 and 11.6 ± 2.34 %ID/g at 48 h post-injection (n=4). Tumor uptake was lowest in the H522 model (4.1 ± 0.98 %ID/g at 48 h post-injection; n=4), while H4006, A549 and H358 exhibited similar uptake of ^{64}Cu-NOTA-YY146. A

---

[*]Corresponding Authors: Weibo Cai, Ph.D., Address: Department of Radiology, University of Wisconsin – Madison, Room 7137, 1111 Highland Ave., Madison, WI 53705-2275, USA. wcai@uwhealth.org; Phone: 608-262-1749; Fax: 608-265-0614., Yunan Yang, M.D., Ph.D., Address: Department of Radiology, University of Wisconsin – Madison, Room 7148, 1111 Highland Ave., Madison, WI 53705-2275, USA. yunan.yang09@gmail.com; Phone: 608-262-1749; Fax: 608-265-0614. .

Conflict of Interest: The authors declare that they have no conflict of interest.

Ethical approval: All applicable international, national, and/or institutional guidelines for the care and use of animals were followed.

positive correlation was found between tumor uptake of ^{64}Cu-NOTA-YY146 (%ID/g) and relative CD146 expression ($r^2=0.98$, $p<0.01$). *Ex vivo* biodistribution corroborated the accuracy of PET data.

Conclusions—The strong correlation between tumor uptake of ^{64}Cu-NOTA-YY146 and CD146 expression demonstrates the potential use of this radiotracer for imaging tumors that elicit varying levels of CD146. In the future, this tool may promote enhanced monitoring of therapeutic response and improved patient stratification.

Keywords

YY146; CD146; Positron emission tomography (PET); lung cancer; monoclonal antibody; molecular imaging

Introduction

Lung cancer is the most commonly diagnosed malignancy worldwide, accounting for more than 13% of all cancers [1]. North America and Europe continue to display the highest incidence rates of lung cancer with 85% of lung cancer malignancies being attributed to smoking [2]. In the United Kingdom, 20% of cancer-related deaths were from lung cancer in 2012 [1]. As cancer treatment has become increasingly personalized in the last decade [3, 4], physicians must determine which patients may benefit from selected therapeutics. For this reason, new tools are needed for imaging malignancies, monitoring therapeutic response, and selecting patients that may benefit from specifically-targeted treatments. Molecular imaging has shown great potential in this field with immunoPET imaging currently leading the domain [5]. ImmunoPET refers to the utilization of positron emission tomography (PET), in combination with highly specific antibody-based imaging tracers, for non-invasively examining tumor phenotypes *in vivo* with high sensitivity and specificity [6].

An epithelial-to-mesenchymal transition (EMT) is a biological process that allows epithelial cells to assume a mesenchymal cell phenotype, effectively gaining migratory and invasive properties [7, 8]. EMT is a major mechanism by which malignant cells gain metastatic potential and resistance to apoptosis signaling pathways; thus, EMT is associated with disease progression and diminished patient survival rates [9, 10]. The cell surface protein called CD146 is an activator of EMTs and overexpression of CD146 in cancer has been shown to down-regulate epithelial markers and upregulate mesenchymal markers [11]. CD146 expression is primarily constrained to the intracellular junctions of endothelial cells and is actively involved in several cellular processes including cell-matrix adhesion, cell migration, signal transduction, stem cell differentiation, immune response, and angiogenesis [12]. Additionally, CD146 has low background levels in normal tissue as well as differential expression in metastases and advanced primary tumors, showing its significant potential in cancer therapy [12, 13]. We have previously shown that persistent and specific targeting of CD146 in vivo may be accomplished with the monoclonal antibody known as YY146 [14].

We previously reported the production of YY146 using a rapid immunization approach that reduced the production time for antibodies by half compared to standard procedures [14]. Cell hybridomas were prepared from B cells collected from the popliteal lymph nodes of mice immunized with the human CD146 antigen. Subsequently, the most immunoreactive antibody clones were determined by ELISA and further evaluated with YY146 showing optimal properties for continued investigation [14]. To date, the use of YY146 has been limited to brain and gastric cancer with both diseases showing high levels of CD146 expression and high uptake of YY146 [13]. PET imaging of YY146 allowed for visualization of small tumor nodules with high specificity in glioblastoma multiforme [14]. To target gastric cancer, superparamagnetic iron oxide nanoparticles (SPIONs) were coated with *d*SiO_2, labeled with near-infrared fluorescence (NIRF) dye ^{800}ZW, and YY146 (^{800}ZW-SPION@*d*SiO_2-YY146) for targeting CD146-expressing gastric cancer [13]. Uptake of ^{800}ZW-SPION@*d*SiO_2-YY146 was rapid and specific allowing for clear delineation of the tumor at 30 min post-injection with the tumor uptake peaking at 24 h post-injection. Both of these studies revealed promising results for the use of YY146 for actively targeting CD146-expressing tumors.

This study provides an investigation of ^{64}Cu-labeled YY146, an antibody targeting human CD146, for imaging of CD146 expression in six mouse models of lung cancer. This was accomplished by evaluating CD146 expression *in vitro* in six human lung cancer cell lines (A549, H358, H522, H4006, H23, and H460) by flow cytometry and Western blot studies. The excellent targeting capabilities of ^{64}Cu-NOTA-YY146 allowed for rapid, persistent, and highly specific accumulation in CD146-expressing tumors. Also, a strong correlation was found between relative CD146-expression and tumor uptake of our imaging tracer, providing the initial evidence supporting the future clinical utilization of ^{64}Cu-NOTA YY146 for enhanced patient stratification or monitoring of therapeutic response.

Materials and Methods

Cell culture

Six human lung cancer cell lines including A549, NCI-H358 (H358), NCI-H522 (H522), HCC4006 (H4006), H23, and NCI-H460 (H460) were obtained from the American Type Culture Collection (ATCC; Manassas, VA, USA). All six cell lines were grown in a humidified incubator at 37 °C with 5% CO_2 using Roswell Park Memorial Institute (RPMI)-1640 medium supplemented with 10% non-heat-inactivated FBS (Gibco, Thermo Fisher Scientific, Waltham, MA, USA) and 1% penicillin-streptomycin solution (Gibco, Thermo Fisher Scientific, Waltham, MA, USA). Cells were used for studies at ~70% confluency.

Animal Models

All animal studies were conducted under a protocol approved by the University of Wisconsin Institutional Animal Care and Use Committee. Subcutaneous xenograft tumors of the six cell lung cancer cell lines (A549, H358, H522, H4006, H23, or H460) were induced in 5-wk-old female athymic nude mice (Crl: NU(NCr)-Foxn1^{nu}; Envigo, Cambridgeshire, United Kingdom). For implantation, 100 μL (1×10^6 cells) of a 1:1 mixture of lung cancer cells and Matrigel Matrix Basement Membrane (Corning, Corning, New York, USA) was subcutaneously injected into the lower flank of the mice. Tumor size was monitored three times weekly, and the animals were used for imaging once the tumor reached 5-10 mm in diameter, which was approximately 3-4 weeks post-implantation.

NOTA conjugation and radiolabeling

The detailed procedures for NOTA conjugation and ^{64}Cu labeling were previously reported [14]. Briefly, a PBS solution of 2-3 mg YY146 was adjusted to pH 8.5-9.0 with 0.1M Na_2CO_3. Next, *p*-SCN-Bn-NOTA (NOTA; Macrocyclics, Dallas, TX, USA) was dissolved in DMSO and immediately added to the antibody solution in a 20:1 molar ratio. The pH was readjusted to 9.0, and the reaction was left to proceed for 2 h at 25-30 °C. Purification of NOTA-YY146 was accomplished using size exclusion PD-10 columns (GE Healthcare, Aurora, OH, USA) with PBS (pH 7.0) as the mobile phase. High specific activity (>5 Ci/μmol at the end of bombardment) ^{64}Cu was produced in a CTI RDS 112 cyclotron via ^{64}Ni(p,n)^{64}Cu reaction. Radiolabeling of the antibody was achieved by reacting 50–100 μg of NOTA-YY146 with 74–148 MBq (2-4 mCi) of ^{64}CuCl2 in 300 μL of 0.1M sodium acetate buffer (pH 4.5) at for 30 min at 37 °C. The resulting tracer, called ^{64}Cu-NOTA-YY146, was purified of free ^{64}Cu using PD-10 columns with PBS as the mobile phase. The radioactive fractions containing ^{64}Cu-NOTA-YY146 were collected and filtered through a 0.2-μm filter for animal injection.

Flow cytometry

The binding and immunoreactivity of YY146 and NOTA-YY146 toward CD146 expressed in six lung cancer cell lines (H4006, H522, H460, H358, H23, and A549) was determined by flow cytometry. Cells were harvested and suspended in ice-cold PBS (pH 7.4) with 1% BSA at a concentration of 1×10^6 cells/mL. Cells were incubated with either PBS, 5 μg/mL of YY146, 25 μg/mL of YY146, 5 μg/mL of NOTA-YY146, or 25 μg/mL of NOTA-YY146 for 30 min at 25-30 °C. After incubation, cells were washed three times with ice-cold PBS and centrifuged at 150 × g for 5 minutes. Next, cells were incubated with the FITC-labeled goat anti-mouse secondary antibody (5 μg/mL) for 30 min at 25-30 °C. After incubation with the secondary antibody, the binding efficiency was analyzed using a MACSQuant cytometer (Miltenyi Biotech, Bergisch Gladbach, Germany) and mean fluorescence intensities were processed using the FlowJo analysis software (Tree Star, Inc., Ashland, OR, USA).

Saturation binding assay

A saturation binding assay was used to calculate the receptor density of CD146 in lung cancer cells. H460 cells were seeded in a 96-well plate at 1×10^6 cells per well. ^{64}Cu-NOTA-YY146 was mixed with non-radiolabeled YY146 at a ratio of 1:1000. Then, the antibody solution was added to each well (0.1 uCi per well) with increasing concentrations (0.03 – 100 nM). After incubation at room temperature for 2 h, cells were washed with 1 × PBS (containing 0.1% BSA) twice, then harvested to determine activity via a gamma counter. To determine the amount of non-specific binding, 1 μmol non-radiolabeled YY146 was added. After 2 hours' incubation at room temperature, cells were washed with 1 × PBS (containing 0.1% BSA) twice and analyzed with a gamma counter. Based on specifically bound ligands, the K_d and B_{max} values were determined, and the receptor density on H460 cells was determined using GraphPad Prism software (La Jolla, CA, USA).

Western blot

CD146 expression was determined by Western blot using standard techniques. Once the lung cancer cell lines reached 70% confluency, the cells were washed with ice-cold PBS. Next, the cells were lysed using Radio Immuno Precipitation Assay (RIPA) buffer (Boston BioProducts, Ashland, MA, USA) supplemented with 1:100 protease inhibitor cocktail (Halt Inhibitor Cocktail, Thermo Fisher Scientific, Carlsbad, CA, USA) for 15 min at 4 °C. Cells were scraped, and the lysis solution was centrifuged at 13,000 ×g for 10 min at 4 °C. The supernatant was removed, and protein concentration was measured using the Pierce™ Coomassie (Bradford) Protein Assay Kit (Thermo Fisher Scientific, Carlsbad, CA, USA). Next, 30 μg of total protein was loaded into the corresponding wells of a 4-12% Bolt Bis-Tris Plus gel (Thermo Fisher Scientific, Carlsbad, CA, USA) in addition to the Chameleon Duo molecular weight ladder (LI-COR Biosciences, Lincoln, NE, USA). Following electrophoresis at 120 mV for 45 min at 4 °C, proteins were transferred to a nitrocellulose membrane using the iBlot 2 system (ThermoFisher Scientific, Carlsbad, CA, USA). The membrane was blocked with Odyssey Blocking Buffer (PBS) (LI-COR Biosciences, Lincoln, NE, USA) for 2 h at 27 °C. The membrane was placed in the iBind Western Device (Thermo Fisher Scientific, Carlsbad, CA, USA) and the primary and secondary antibody solutions and washes were put in the corresponding chambers. Dilutions of 1:100 and 1:400 were made of the mouse-derived monoclonal CD146 antibody (Santa Cruz, Dallas, TX, USA) and rabbit β-actin (LI-COR Biosciences, Lincoln, NE, USA) were made with the iBind Fluorescent Detection Solution Kit (Thermo Fisher Scientific, Carlsbad, CA, USA) according to the manufacturer's protocol. Similarly, the secondary antibodies (donkey anti-mouse IRDye 680RD and donkey anti-human 800CW) were diluted at 1:1500 and placed into their corresponding chamber. The membrane was left in the iBind system for 12 h at 4 °C before the membrane was removed for scanning using the LI-COR Odyssey Infrared Imaging System (LI-COR Biosciences, Lincoln, NE, USA).

PET imaging and image analysis

PET scans were performed at 4, 24, and 48 h after mice were injected with ^{64}Cu-NOTA-YY146 on the Inveon microPET rodent model scanner (Siemens Medical Solutions, Malvern, PA, USA). Anesthesia was induced and maintained with 2% isoflurane, and mice were placed in the scanner in the prone position for imaging. At each time point, 20 million coincidence events were acquired per mouse for every static PET emission scan (energy window, 350–650 keV; time window, 3.432 ns; resolution, 1.5 mm). Image reconstructions of PET scans were performed using the Inveon Acquisition Workplace (Siemens Medical Solutions, Malvern, PA, USA). Quantitative region-of-interest (ROI) analysis of the PET images was carried out on the attenuation and decay corrected PET images, and the uptake of activity in tissues was presented as the percentage of injected dose per gram (%ID/g).

Correlation between CD146 expression and tumor uptake of ^{64}Cu-NOTA-YY146

The CD146/β-actin ratio of CD146 expression and relative expression of CD146 were correlated with the tumor uptake of ^{64}Cu-NOTA-YY146 in the six lung cancer-derived tumor models. The Origin 2015 software (Origin Labs, Northampton, MA, USA) was used to plot the average values for uptake of ^{64}Cu-NOTA-YY146 in each model (n=4-5) against the quantified levels of CD146 determined by Western blot studies. A linear fit was applied to the graph to determine the strength of the association between tumor uptake of our imaging probe and expression levels, also known as the correlation coefficient (r^2).

Ex vivo biodistribution studies

Biodistribution studies were performed to validate the PET data after the final PET scans 48 h after injection. Mice were euthanized by CO_2 asphyxiation before the blood, tumor, and all the main organ/tissues were collected and weighed. The activity in tissues was counted in an automated γ-counter (PerkinElmer, Waltham, MA, USA), and the accumulated activity values were calculated and reported as %ID/g (mean ± SD).

Immunofluorescence staining

Immunofluorescence staining was conducted following a previously described methodology to evaluate the expression of CD146 and CD31 in tumor sections of six lung cancer models [15]. Briefly, tumors extracted after the last PET imaging time point (48 h) and embedded in Tissue-Tek optimal cutting temperature (O.C.T.) compound (Sakura Finetek, Torrance, CA, USA). Histologic sectioning of tumor tissue was provided by the University of Wisconsin Carbone Cancer Center Experimental Pathology Laboratory. Frozen tissue slices of 5-μm thickness were fixed with cold acetone for 10 min and dried in the air for 30 min. PBS was used to rinse the slides before slides were blocked with 10% donkey serum for 30 min at 25 °C. Next, the slides were incubated overnight at 4 °C with 1 mL of YY146 (10 μg/mL) and 1 mL of rat anti-mouse CD31 (BD BioSciences, San Jose, CA, USA) antibody (2 μg/mL). AlexaFluor$_{488}$-labeled goat anti-mouse antibody and Cy3-labeled donkey anti-rat antibodies were used to visualize CD146 and CD31, respectively. A coverslip was applied to each slide using Vectashield mounting medium for fluorescence microscopy with DAPI (4′, 6-diamidino-2-phenylindole) (Vector Laboratories, Burlingame, CA, USA). All images were acquired using an A1R confocal microscope (Nikon). All images were acquired with a Nikon Digital Eclipse C1 plus microscope equipped with three excitation lasers at 488 nm, 546 nm, and 633 nm (Nikon Instruments, Melville, NY, USA).

Tissue Microarray Analysis

The FDA normal human organ tissue array (FDA993; US Biomax, Inc., Rockville, MD, USA) and multi-type lung cancer and normal tissue with TNM and grade tissue microarray (LCM501; US Biomax, Inc., Rockville, MD, USA) were stained for CD146 expression. Briefly, the slides were deparaffinized through xylene and ethanol washes before antigen retrieval using Vector Antigen Unmasking solution (Vector Laboratories, Burlingame, CA, USA). Next, slides were blocked with 2.5% normal horse serum of the Impress Reagent Kit Anti-Mouse IgG (Vector Laboratories, Burlingame, CA, USA) for 30 min at room temperature. The slides were incubated with the primary anti-CD146 antibody (NBP2-44512; Novus Biologicals, Littleton, CO, USA) overnight at 4 °C. Slides were washed with PBS and blocked with 3% H_2O_2 for 5 min. Next, slides were incubated with the ImmPACT DAB reagent (Vector Laboratories, Burlingame, CA, USA) for 45 s. Slides were rinsed 0.05 M sodium bicarbonate solution (pH 9.6) for 10 min before DAB Enhancement solution (Vector Laboratories, Burlingame, CA, USA) was added for 20 s before the slides were washed and counterstaining with Hematoxylin QS (Vector

Laboratories, Burlingame, CA, USA) for 20 s. Slides were washed several times in water and coverslipped for microscopic analysis. Staining intensity was determined using ImageJ and tissues were categorized as 0 for no positive staining, 1 for light positive staining, 2 for moderate positive staining, and 3 for high positive staining. To calculate the percent positive, 0 and 1 were considered as CD146 negative, while 2 and 3 were considered CD146 positive.

Statistical Analysis

Quantitative data were expressed as mean ± standard deviation (SD). Statistical analyses were performed using a Student t-test or one-way analysis of variance (ANOVA). A confidence interval of 95% was selected with $p<0.05$ considered statistically significant.

Results

Binding of YY146 and NOTA-YY146 to CD146

The binding of YY146 to CD146-expressing cells was analyzed by flow cytometry **(**Fig. 1**)**. Cell lines were incubated with YY146 (5 or 25 μg/mL), NOTA-conjugated YY146 (5 or 25 μg/mL), secondary antibody alone, or PBS as a negative control. H460 and H23 cells displayed enhanced fluorescence signal when incubated with both YY146 and NOTA-YY146, indicative of elevated CD146 expression in these cell lines. Also, there were no appreciable differences in the binding affinity of NOTA-YY146 or YY146 alone, suggesting that NOTA-conjugation did not affect the immunoreactivity of YY146 to CD146 at either concentration. A549 and H4006 cells showed similar results to H460 and H23, yet at a lesser degree which suggests lower levels of CD146 expression in these two cell lines. H358 cells showed a slight increase in fluorescence signal when incubated with 25 μg/mL of YY146 or NOTA-YY146, yet the lower concentration of YY146 or NOTA-YY146 (5 μg/mL) failed to provide a signal difference. This suggests that H358 cells express CD146 at low levels. Lastly, H522 cells did not display an increase in fluorescence signal when incubated with YY146 or NOTA-YY146, indicating that this cell line may lack CD146 or the cell line may display basal levels of CD146 expression.

CD146 expression in lung cancer cell lines

The expression of CD146 was examined in six human lung cancer cell lines. Western blot results were quantified using a protocol provide by LiCor technologies [16]. The ratio of CD146 to β-actin was calculated in addition to the relative expression of CD146 **(**Fig. 2 and Table S1**)**. The ratio of CD146 to β-actin was obtained by normalizing the band intensities of CD146 to β-actin while relative CD146 expression shows the values not normalized to B-actin levels. Two bands were seen in each Western blot at ~110 kDa corresponding to CD146 while β-actin was visible at 38 kDa (Fig. 2a). In each case, the band for H460 cell line displayed the highest signal (relative expression of CD146 is normalized to 1.00), indicative of the highest CD146 expression (n=3; Fig. 2b-c). H522 and H4006 showed similar expression levels of CD146 with relative expression values of 0.34 ± 0.05 and 0.25 ± 0.02, respectively (n=3; Fig. 2c). H23 cells displayed lower levels of relative CD146 expression (0.18 ± 0.03), while A549 and H358 showed background or minimal expression of CD146 with relative expression values of 0.06 ± 0.01 and 0.07 ± 0.01, respectively (n=3;

Fig. 2c). CD146 expression receptor density was calculated for H460, which expressed the highest level of CD146, and determined to be ~125,000 receptors per cell (Fig. S1).

ImmunoPET imaging of ^{64}Cu-NOTA-YY146 in six tumor models

The biodistribution of ^{64}Cu-NOTA-YY146 was monitored in lung cancer-derived mouse models for 48 h post-injection. Representative maximum intensity projection (MIP) images were provided from each group of tumor-bearing mice at 4, 24, and 48 h post-injection **(**Fig. 3**)**. For each group, the artery (A), heart (H), liver (L), spleen (S), and tumor (T) have been denoted. PET imaging revealed different degrees of ^{64}Cu-NOTA-YY146 between the six mouse models with H460 and H23 tumors showing the highest tracer accumulation. Most tumor models, excluding H358 and H522, showed prominent uptake of ^{64}Cu-NOTA-YY146 that allowed for clear delineation of tumor boundaries. All mouse models displayed similar blood uptake suggesting that the antibody was highly stable in circulation. Also, high tracer accumulation in the liver was indicative of the hepatic clearance and possible hepatobiliary circulation that antibodies undergo for clearance.

The ROI quantitative analysis of PET images revealed high activity in the blood pool that steadily declined throughout the study for each tumor-derived model **(**Fig. 4 and Tables S2-S4**)**. At 4 h post-injection, activity in the blood pool was between 17.5 ± 1.49 and 20.5 ± 0.78 %ID/g (n=4; Fig. 4b). Also, initially high levels of activity in liver tissues were linked to the slow clearance mechanism displayed by intact IgG antibodies [17]. Both the liver and spleen displayed high levels of activity at 4 h post-injection, yet these values gradually decreased between 24 and 48 h post-injection **(**Fig. 4**)**. Tumor accumulation of ^{64}Cu-NOTA-YY146 was highest in the H460 tumor model at 4, 24, and 48 h post-injection with activity levels of 10.5 ± 1.97, 17.4 ± 2.41, and 20.1 ± 2.86 %ID/g, respectively (n=4; Fig. 4a). Activity in the tumor was shown to increase in each cell line, yet accumulation in CD146 negative cell lines suggests a minimal amount of non-specific accumulation attributed to the enhanced permeability and retention (EPR) effect.

The ratios of activity between tumor and muscle tissues were calculated to compare the six different models **(**Fig. S2**)**. Several statistically significant differences were found between the six tumor models, with H460 displaying statistically significant differences in activity accumulation between each of the other tumor models at 48 h post-injection (n=4; $^{*}p<0.05$, $^{**}p<0.01$; Fig. S2). Also, statistically significant differences were found between the tumor-to-muscle of H23 and three other tumor models (H4006, H358, and H522) at 48 h post-injection (n=4; $^{*}p<0.05$, $^{**}p<0.01$).

Correlation between CD146 expression and uptake of ^{64}Cu-NOTA-YY146

Quantitative data from ROI analysis and Western blot studies were used to investigate the correlation between the uptake of ^{64}Cu-NOTA-YY146 (%ID/g) and CD146 expression levels **(**Fig. 5**)**. A strong linear correlation was found between the tumor accumulation of the imaging probe and CD146/β-actin ratio at 48 h post-injection (r^2=0.96, p<0.01; Fig. 5a). Similarly, tumor accumulation of ^{64}Cu-NOTA-YY146 and relative CD146 expression displayed a strong linear correlation at 48 h post-injection (r^2=0.98, p<0.01; Fig. 5b).

Biodistribution of ^{64}Cu-NOTA-YY146

Ex vivo biodistribution was carried out after the final PET imaging time point at 48 h post-injection to validate the uptake values determined from PET ROI analysis **(**Fig. 6**)**. At this time, mice were euthanized, and the tumor, blood, and majors organs were collected for gamma counting. Biodistribution of ^{64}Cu-NOTA-YY146 in tumor-bearing mice revealed high blood uptake that was similar between all six tumor models, further validating the serum stability of the imaging tracer (n=4; Table S5). Elevated uptake of ^{64}Cu-NOTA-YY146 was also found in liver, kidney, and spleen tissues with intramodel similarities. Several organs and tissues displayed minimal or background levels of activity, including the pancreas, stomach, bone, muscle, and brain. Also, biodistribution studies corroborated the variations in tumor uptake of ^{64}Cu-NOTA-YY146 originally established by PET imaging. A statistically significant difference in tumor uptake was found between H460 and the other cell line-derived tumor models (Fig. 6; n=4; $p<0.05$). Also, H23 tumors displayed higher uptake of ^{64}Cu-NOTA-YY146 then H4006, A549, H358, and H522 tumors (Fig. 6; n=4; $p<0.05$). Overall, *ex vivo* biodistribution studies provided physical evidence supporting the accuracy of PET imaging analysis for quantifying the biodistribution of ^{64}Cu-NOTA-YY146 *in vivo*, providing deeper insight into the movement of highly specific radiolabeled tracers injected into tumor-derived mouse models.

Immunofluorescence co-staining of CD146 and CD31

Ex vivo immunofluorescence staining of tumor sections for CD146 and CD31 provided further insight into the spatial location of CD146 in each tumor model while also offering details regarding tumor vasculature. The cell lines were shown to express CD146 by immunofluorescence staining **(**Fig. 7**)**. Expression of CD146, as shown in the green fluorescence channel, was highest in H460 tumor sections closely followed by H23. The A549, H522, and H358 tumor sections exhibited low fluorescence signal which is suggestive of median to low levels of CD146 expression. Lastly, H4006 tumor sections showed no fluorescence staining of CD146 indicative of minimal CD146 expression. In addition to CD146, CD31 was stained for visualization of tumor vasculature. Each tumor model displayed similar levels of vasculature, yet the vasculature appeared more organized in some tumor models including H460, H23, A549, andH4006 **(**Fig. 7**)**. Together, these results from the immunofluorescence staining of *ex vivo* tumor sections further verify the findings from *in vivo* assays, PET imaging, and biodistribution studies.

CD146 staining of normal human tissues and human lung malignancies

Tissue microarrays were used to examine the overall expression of CD146 in both NSCLC and SCLC (Fig. S3). It was determined that that 74.4% of NSCLC showed high CD146 expression, while only 20.0% of SCLC showed high CD146 expression. In addition, CD146 was found to be expressed in several healthy tissues, including the tonsils, stomach, kidneys, larynx, uterus, liver, and some nerve tissues (Fig. S4). These results were in agreement with observations found by the Human Protein Atlas [18].

Discussion

Despite significant diagnostic and therapeutic advancements, lung cancer remains the leading cause of cancer-related death worldwide [19]. As lung tumors display phenotypic and genotypic heterogeneities between patients [20, 21], it has become increasingly important for physicians to construct individualized treatment plans effective for each patient. In the last decade, the role of genomic screening in cancer clinics has become conventional, as studies have shown that over 60% of patients with lung cancer display one or more specific mutations [22]. The results from genomic testing may have a significant impact on individual treatment plans. For example, patients with an epidermal growth factor receptor (EGFR) mutation experience a higher response rate to erlotinib [23], while crizotinib is considered for patients with the fusion gene echinoderm microtubule-associated protein like 4 - anaplastic lymphoma kinase (EML4-ALK) [24]. Genomic screening is an extremely invasive procedure requiring tissue biopsies; thus, researchers are assessing newer technologies, like molecular imaging, for non-invasively assessing tumor phenotypes in patients.

Recently, CD146 overexpression was evaluated in high-grade gliomas by molecular imaging [14]. While the antibody showed high specificity in CD146-expressing gliomas, the study did not correlate CD146 expression with tumor uptake. As antibody tracers are specifically targeted to their corresponding protein, previous studies have shown that a receptor density of greater than 10^5 receptors per cell is required for effective targeting [25, 26]. CD146 was previously found to be expressed in 51% of human lung cancer malignancies, correlating with shortened survival for patients with adenocarcinomas [27]. In this study, we confirmed through microarray analysis that CD146 was expressed in 74.4% of patient samples, yet CD146 was only expressed in 20% of SCLC (Fig. S3). Another study corroborated these findings by showing that patient survival was decreased from 84% to 50% for patients with tumors expressing CD146 [28]. For these reasons, CD146 has become an attractive biomarker for predicting patient survival, stratification of cancer patients, and the development of CD146-targeted therapies. While an imaging agents based upon CD146 alone may be limited for clinically detecting all lung malignancies, it may provide both diagnostic and monitoring benefits to many patients. In addition, imaging biomarkers provide an alternative to highly invasive tissue biopsies.

In this study, we hypothesized that tumor uptake of ^{64}Cu-NOTA-YY146 would strongly correlate with the tumor expression of CD146. Quantification of the protein bands on Western blot provided numerical values for both relative expression and β-actin normalized expression **(**Table S1**)**. We found that the relative CD146 expression values displayed the strongest correlation between tumor uptake of ^{64}Cu-NOTA-YY146 and CD146 expression (r^2=0.98, p<0.01; Fig. 5b) while β-actin normalized values provided a slightly weaker correlation (r^2=0.96, p<0.01; Fig. 5a). As cell lines may display marginally different levels β-actin [29], it was not alarming that the relative expression showed a stronger correlation.

Radiolabeling of YY146 with ^{64}Cu required the use of NOTA, which is conjugated to the antibody via lysine residues. As shown by flow cytometry and immunofluorescence staining studies (Fig. 1 and Fig. 7), conjugation of this chelator did not impair the binding of YY146 to CD146. This suggests that the lysine residues involved in the conjugation chemistry were not involved in the binding sites of YY146 [30-33]. Overall, PET imaging revealed that tumor uptake of ^{64}Cu-NOTA-YY146 was persistent, prominent, and highly specific.

Tumor accumulation of the antibody tracer was highest in H4006 and H23 tumor models at 48 h (20.1 ± 2.86 and 11.6 ± 2.34 %ID/g, respectively; n=4; Fig. 4a). While it is possible that passive accumulation of the antibody tracer could attribute to these values as a result of the enhanced permeability and retention (EPR) effect, previous studies have showed that off target accumulation usually occurs faster (<24 h) and tumors will display a slow decrease in %ID/g [34, 35]. In our study, the maximum tumor uptake of ^{64}Cu-NOTA-YY146 occurred at the final time point (48h), showing a plateau in %ID/g with no leakage or decline in activity **(**Fig. 4**)**. Uptake of the tracer in the blood pool was initially high ranging from 17.4 ± 1.12 to 20.5 ± 0.78 %ID/g at 4 h post-injection (n=4) with a steady decline over time **(**Fig. 4b**)**. As antibodies may circulate for up to 45 days *in vivo* [36], we expected to see high blood activity levels as it verified the enhanced stability of our tracer for *in vivo* applications.

Conclusions

This study describes the characterization of ^{64}Cu-labeled YY146, an antibody specifically targeting human CD146, in six mouse models of human lung cancer. PET imaging revealed high uptake of ^{64}Cu-NOTA-YY146 in CD146-positive tumors while tumor models with low CD146 expression displayed significantly less tumor uptake. Also, a strong linear correlation was found between tumor uptake of ^{64}Cu-NOTA-YY146 and relative expression of CD146 in the tumor cell lines (r^2=0.98, p<0.01), reinforcing the potential employment of immunoPET imaging for quantitatively assessing CD146 expression *in vivo*. Since CD146 is expressed in many cancer, we believe that CD146-based tracers may show may great clinical utility in the future, as this versatile imaging agents may assist in diagnosing or staging cancers, monitoring patients' therapeutic response, or investigating novel therapeutic and diagnostic antibodies.

Supplementary Material

Refer to Web version on PubMed Central for supplementary material.

Acknowledgments

This work is supported, in part, by the University of Wisconsin - Madison, the National Institutes of Health (NIBIB/NCI 1R01CA169365, P30CA014520, T32CA009206, and T32GM008349), the National Science Foundation (DGE-1256259), and the American Cancer Society (125246-RSG-13-099-01-CCE).

References

1. Torre LA, Bray F, Siegel RL, Ferlay J, Lortet-Tieulent J, Jemal A. Global cancer statistics, 2012. CA Cancer J Clin. 2015; 65(2):87–108. [PubMed: 25651787]
2. Cosaert J, Quoix E. Platinum drugs in the treatment of non-small-cell lung cancer. Br J Cancer. 87(8):825–33. 220. [PubMed: 12373594]
3. Miranda DM, Mamede M, Souza BR, Almeida Barros AG, Magno LA, Alvim-Soares A Jr, et al. Molecular medicine: a path towards a personalized medicine. Rev Bras Psiquiatr. 2012; 34(1):82–91. [PubMed: 22392394]

4. Hamburg MA, Collins FS. The path to personalized medicine. N Engl J Med. 2010; 363(4):301–4. [PubMed: 20551152]
5. Knowles SM, Wu AM. Advances in immuno-positron emission tomography: antibodies for molecular imaging in oncology. J Clin Oncol. 2012; 30(31):3884–92. [PubMed: 22987087]
6. van Dongen GA, Visser GW, Lub-de Hooge MN, de Vries EG, Perk LR. Immuno-PET: a navigator in monoclonal antibody development and applications. Oncologist. 2007; 12(12):1379–89. [PubMed: 18165614]
7. Fischer KR, Durrans A, Lee S, Sheng J, Li F, Wong ST, et al. Epithelial-to-mesenchymal transition is not required for lung metastasis but contributes to chemoresistance. Nature. 2015; 527(7579): 472–6. [PubMed: 26560033]
8. Larue L, Bellacosa A. Epithelial-mesenchymal transition in development and cancer: role of phosphatidylinositol 3[prime] kinase//AKT pathways. Oncogene. 2005; 24(50):7443–54. [PubMed: 16288291]
9. Cho JY. Molecular diagnosis for personalized target therapy in gastric cancer. J Gastric Cancer. 2013; 13(3):129–35. [PubMed: 24156032]
10. Kalluri R, Weinberg RA. The basics of epithelial-mesenchymal transition. J Clin Invest. 2009; 119(6):1420–8. [PubMed: 19487818]
11. Zeng Q, Li W, Lu D, Wu Z, Duan H, Luo Y, et al. CD146, an epithelial-mesenchymal transition inducer, is associated with triple-negative breast cancer. Proc Natl Acad Sci U S A. 2012; 109(4): 1127–32. [PubMed: 22210108]
12. Wang Z, Yan X. CD146, a multi-functional molecule beyond adhesion. Cancer Lett. 2013; 330(2): 150–62. [PubMed: 23266426]
13. Wang P, Qu Y, Li C, Yin L, Shen C, Chen W, et al. Bio-functionalized dense-silica nanoparticles for MR/NIRF imaging of CD146 in gastric cancer. Int J Nanomedicine. 2015; 10:749–63. [PubMed: 25653520]
14. Yang Y, Hernandez R, Rao J, Yin L, Qu Y, Wu J, et al. Targeting CD146 with a 64Cu-labeled antibody enables in vivo immunoPET imaging of high-grade gliomas. Proc Natl Acad Sci U S A. 2015; 112(47):E6525–34. [PubMed: 26553993]
15. Luo H, England CG, Graves SA, Sun H, Liu G, Nickles RJ, et al. PET Imaging of VEGFR-2 Expression in Lung Cancer with 64Cu-Labeled Ramucirumab. J Nucl Med. 2016; 57(2):285–90. [PubMed: 26541778]
16. Eaton SL, Hurtado ML, Oldknow KJ, Graham LC, Marchant TW, Gillingwater TH, et al. A guide to modern quantitative fluorescent western blotting with troubleshooting strategies. J Vis Exp. 2014; (93):e52099. [PubMed: 25490604]
17. Wang W, Wang EQ, Balthasar JP. Monoclonal antibody pharmacokinetics and pharmacodynamics. Clin Pharmacol Ther. 2008; 84(5):548–58. [PubMed: 18784655]
18. Uhlen M, Fagerberg L, Hallstrom BM, Lindskog C, Oksvold P, Mardinoglu A, et al. Proteomics. Tissue-based map of the human proteome. Science. 2015; 347(6220):1260419. [PubMed: 25613900]
19. ACS. Cancer Facts & Figures 2016. American Cancer Society; Atlanta: 2016.
20. Tripodis N, Demant P. Genetic analysis of three-dimensional shape of mouse lung tumors reveals eight lung tumor shape-determining (Ltsd) loci that are associated with tumor heterogeneity and symmetry. Cancer Res. 2003; 63(1):125–31. [PubMed: 12517788]
21. Marusyk A, Polyak K. Tumor heterogeneity: causes and consequences. Biochim Biophys Acta. 2010; 1805(1):105–17. [PubMed: 19931353]
22. Esposito L, Conti D, Ailavajhala R, Khalil N, Giordano A. Lung Cancer: Are we up to the Challenge? Curr Genomics. 2010; 11(7):513–8. [PubMed: 21532835]
23. Wang Y, Schmid-Bindert G, Zhou C. Erlotinib in the treatment of advanced non-small cell lung cancer: an update for clinicians. Ther Adv Med Oncol. 2012; 4(1):19–29. [PubMed: 22229045]
24. Sahu A, Prabhash K, Noronha V, Joshi A, Desai S. Crizotinib: A comprehensive review. South Asian J Cancer. 2013; 2(2):91–7. [PubMed: 24455567]
25. Jarantow SW, Bushey BS, Pardinas JR, Boakye K, Lacy ER, Sanders R, et al. Impact of Cell-surface Antigen Expression on Target Engagement and Function of an Epidermal Growth Factor

Receptor x c-MET Bispecific Antibody. J Biol Chem. 2015; 290(41):24689–704. [PubMed: 26260789]

26. Perez HL, Cardarelli PM, Deshpande S, Gangwar S, Schroeder GM, Vite GD, et al. Antibody-drug conjugates: current status and future directions. Drug Discov Today. 2014; 19(7):869–81. [PubMed: 24239727]
27. Kristiansen G, Yu Y, Schluns K, Sers C, Dietel M, Petersen I. Expression of the cell adhesion molecule CD146/MCAM in non-small cell lung cancer. Anal Cell Pathol. 2003; 25(2):77–81. [PubMed: 12632016]
28. Oka S, Uramoto H, Chikaishi Y, Tanaka F. The expression of CD146 predicts a poor overall survival in patients with adenocarcinoma of the lung. Anticancer Res. 2012; 32(3):861–4. [PubMed: 22399604]
29. Nowak D, Skwarek-Maruszewska A, Zemanek-Zboch M, Malicka-Blaszkiewicz M. Beta-actin in human colon adenocarcinoma cell lines with different metastatic potential. Acta Biochim Pol. 2005; 52(2):461–8. [PubMed: 15940343]
30. Sugiura G, Kuhn H, Sauter M, Haberkorn U, Mier W. Radiolabeling strategies for tumor-targeting proteinaceous drugs. Molecules. 2014; 19(2):2135–65. [PubMed: 24552984]
31. Vosjan MJ, Perk LR, Visser GW, Budde M, Jurek P, Kiefer GE, et al. Conjugation and radiolabeling of monoclonal antibodies with zirconium-89 for PET imaging using the bifunctional chelate p-isothiocyanatobenzyl-desferrioxamine. Nat Protoc. 2010; 5(4):739–43. [PubMed: 20360768]
32. Gooden CS. Radiolabeling of monoclonal antibodies. Methods Mol Med. 2000; 40:341–50. [PubMed: 21337105]
33. Rogers BE, Anderson CJ, Connett JM, Guo LW, Edwards WB, Sherman EL, et al. Comparison of four bifunctional chelates for radiolabeling monoclonal antibodies with copper radioisotopes: biodistribution and metabolism. Bioconjug Chem. 1996; 7(4):511–22. [PubMed: 8853465]
34. Cai W, Chen K, He L, Cao Q, Koong A, Chen X. Quantitative PET of EGFR expression in xenograft-bearing mice using 64Cu-labeled cetuximab, a chimeric anti-EGFR monoclonal antibody. Eur J Nucl Med Mol Imaging. 2007; 34(6):850–8. [PubMed: 17262214]
35. Cai W, Wu Y, Chen K, Cao Q, Tice DA, Chen X. In vitro and in vivo characterization of 64Cu-labeled Abegrin, a humanized monoclonal antibody against integrin alpha v beta 3. Cancer Res. 2006; 66(19):9673–81. [PubMed: 17018625]
36. Petkova SB, Akilesh S, Sproule TJ, Christianson GJ, Al Khabbaz H, Brown AC, et al. Enhanced half-life of genetically engineered human IgG1 antibodies in a humanized FcRn mouse model: potential application in humorally mediated autoimmune disease. Int Immunol. 2006; 18(12): 1759–69. [PubMed: 17077181]

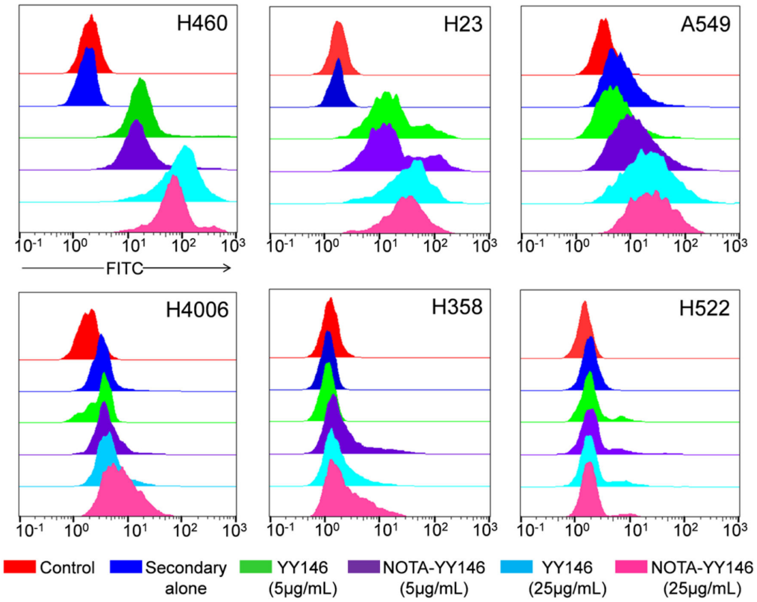

Fig. 1.

Flow cytometry analysis of six lung cancer cell lines with YY146 and NOTA-YY146. Each cell line was incubated with PBS (control; red), secondary antibody alone (blue), 5 μg/mL YY146 (green), 5 μg/mL NOTA-YY146 (purple), 25 μg/mL YY146, or 25 μg/mL NOTA-YY146 to determine CD146 expression and YY146 immunoreactivity.

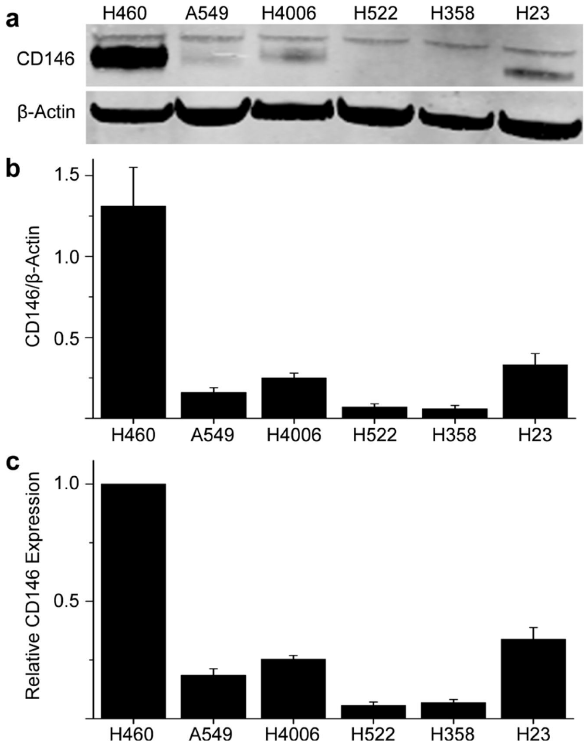

Fig. 2.

CD146 expression in six lung cancer cell lines determined by Western blot. (a) The membrane was incubated with primary antibodies (monoclonal CD146 antibody and rabbit β-actin antibody) and secondary antibodies (donkey anti-mouse IRDye 680RD and donkey anti-human 800CW). A band corresponding to CD146 was visualized ~110 kDa while β-actin displayed a prominent band at ~43 kDa. (b) The ratio of CD146 to β-actin was calculated by normalizing CD146 to their corresponding β-actin band (n=3). (c) Relative CD146 expression values were not normalized to β-actin (n=3)

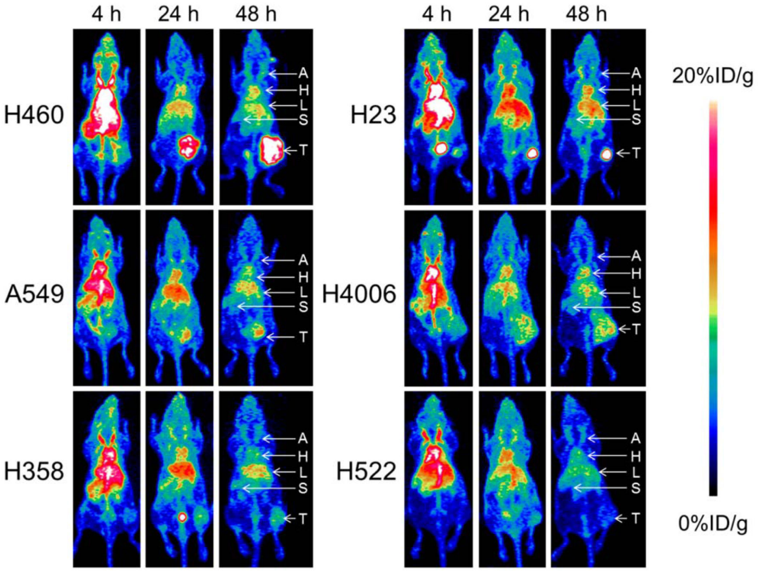

Fig. 3.

Maximum intensity projections (MIPs) of sequential PET images in lung cancer-derived tumor-bearing mice at 4, 24, and 48 h post-injection (n=4). The arteries (A), heart (H), liver (L), spleen (S), and tumor (T) are indicated by arrows

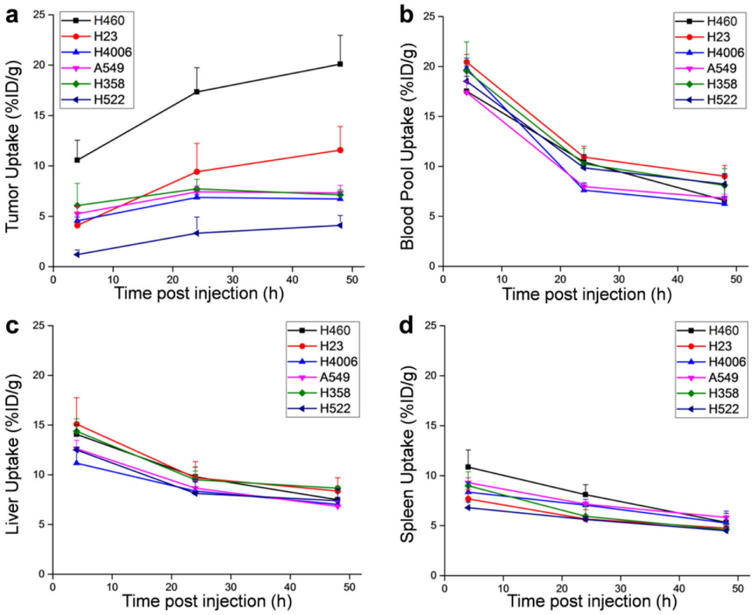

Fig. 4.

Time-activity curves showing ^{64}Cu-NOTA-YY146 uptake in (a) tumor, (b) blood pool, (c) liver, and (d) spleen tissues determined by PET ROI analysis (n=4)

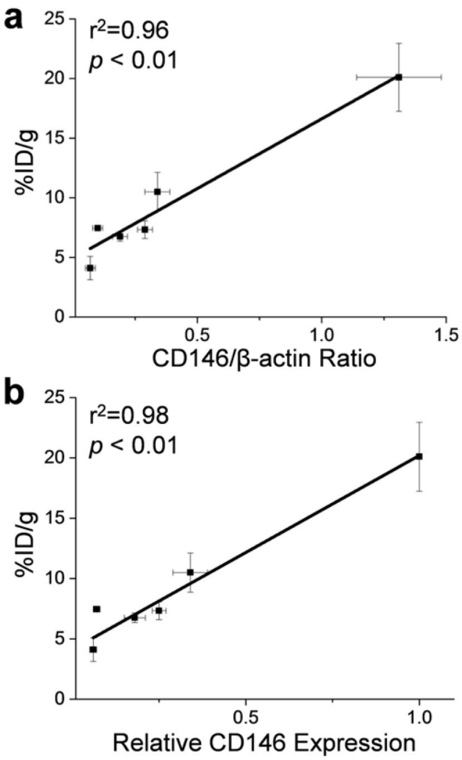

Fig. 5.

Correlation between tumor uptake (%ID/g) and CD146-expression in lung cancer cell lines. Tumor uptake was correlated with (a) the ratio of CD146 to β-actin and (b) the relative expression of CD146

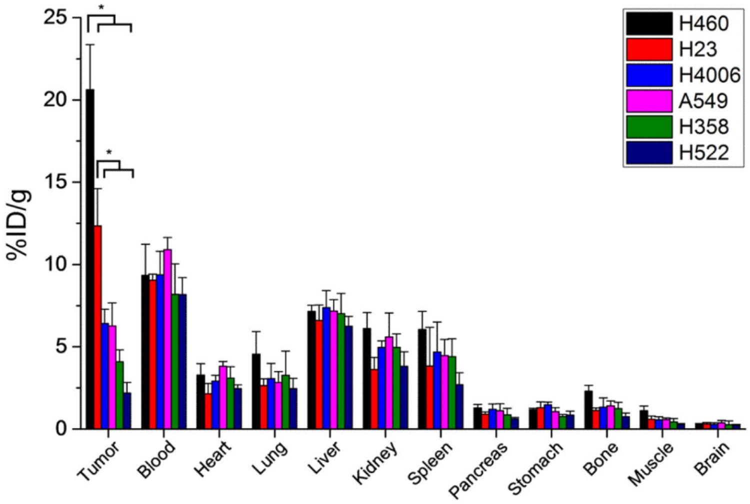

Fig. 6.

Ex vivo biodistribution of ^{64}Cu-NOTA-YY146 in lung cancer mouse models at 48 h post-injection (n=4)

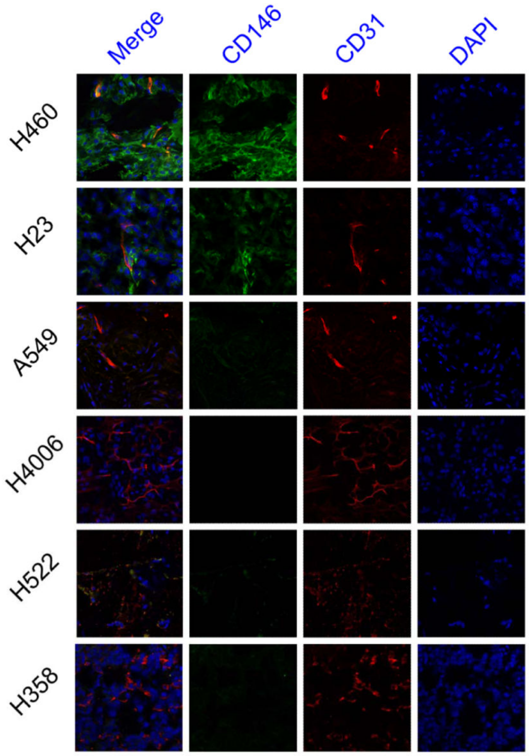

Fig. 7.

Immunofluorescence co-staining of tumor sections for CD146 and CD31. The two primary antibodies, YY146 (green) and CD31 (red), were visualized with AlexaFluor$_{488}$-labeled goat anti-mouse and Cy3-labeled donkey anti-rat secondary antibodies. Cell nuclei were stained with DAPI (blue). Magnification 400X